Desalination and Water Treatment
www.deswater.com

doi: 10.1080/19443994.2013.822171

51 (2013) 6459–6471
October

Taylor & Francis
Taylor & Francis Group

Modeling mass transfer using surface morphology in full-scale reverse osmosis membrane processes

Yuming Fang, Steven J. Duranceau*

Department of Civil, Environmental and Construction Engineering, University of Central Florida, PO Box 162450, Orlando, FL 32816 2450, USA
Tel. +1 407 823 1440; Fax: +1 407 823 3315; email: steven.duranceau@ucf.edu

Received 24 April 2013; Accepted 23 May 2013

ABSTRACT

The influence of surface characteristics on membrane process performance is considered significant and is not well understood. Current mass transport models generally assume constant mass transfer coefficients (MTCs) based on a homogeneous flat surface. This study evaluated membrane mass transfer by incorporating surface morphology into a diffusion-based model assuming that the MTCs are dependent on the thickness variation of the membrane's active layer. Concentration polarization is also affected by this nonuniform surface property and was incorporated into the model. A simulation was performed using parameters from a full-scale 4.5 million gallon per day brackish water reverse osmosis membrane process. The process was simulated by modeling one thousand uniform slices of the membrane channel and the permeate water quality was determined locally through a finite difference approach. It was determined that solute mass transport is controlled by diffusion in the nonhomogeneous thinner regions (membrane valleys) of the active layer. This nonuniform surface affected the concentration polarization layer, where more solutes tended to accumulate within the valleys than on the ridges. Prediction of the permeate total dissolved solids concentration was accurate, ranging between 5 and 15%, as measured as an average percent difference between predicted and actual values.

Keywords: Membrane active-layer; Reverse osmosis; Mass transfer coefficients; Concentration polarization; Mathematical models

1. Introduction

Reverse osmosis (RO) membranes represent an important set of pressure driven processes for domestic and industrial water treatment. [1–4]. The majority of RO membranes are manufactured in a spiral wound configuration using thin-film composite (TFC) technologies. Studies have shown that TFC membranes consist of three layers: a microscopically-thin active polyamide layer surface, a microporous polysulfone backing layer, and a polyester support layer. The polysulfone and polyester layers serve to support the thin-film application, while the polyamide layer is the portion of the composite actively participating in the rejection of dissolved solutes [5,6]. There have been many studies in which the relationship between the surface structure and membrane permeability has been examined. Bason investigated ion exclusion mechanisms in the polyamide layer of

*Corresponding author.

membranes. They concluded that the film did not behave as an ideal planar homogeneous layer. Observations regarding ion transport were in disagreement with this idealized model, which assumed a uniform structure of the thin film [7]. Mendret developed a theoretical model to predict growth of solid deposits on a nonuniform permeable membrane [8]. Zhao and Taylor investigated the impact of both membrane surface properties and natural organic matter on membrane performance [9]. With the application of Atomic Force Microscopy (AFM), membrane surface characteristics such as surface morphology, pore sizes, surface porosity can be determined and correlated with membrane performance. The AFM images presented in the study of Vrijerhoek depict membrane surfaces as having an elevated ridge and depressed valley morphology. They concluded the fouling behavior was related to the degree of surface roughness [10]. In addition, AFM was used to reveal images of membrane surface structures and differentiate between "rough" and "smooth" membranes. These studies suggested that membrane permeability was indeed affected by the surface morphology; however, a method to numerically represent the membrane surface structure, and its impact on solute mass transfer has yet to be developed.

Concentration polarization affects permeability in spiral wound RO membrane, where water flows tangentially to the membrane surface. As water selectively permeates the membrane, the retained solutes accumulate at the membrane solution interface. Thus, a concentration gradient between the solution at the bulk and the membrane surface is established that results in the back diffusion of the solute accumulated at the membrane surface. This phenomenon is referred to as concentration polarization. In RO membrane processes, concentration polarization leads to an increase in the osmotic pressure that is directly related to the solute concentration at the membrane surface. At constant applied hydrostatic pressure, the increase in osmotic pressure will cause a decrease in permeate flux. The problem of concentration polarization at the membrane surface has been investigated by Brain [11], Marina [12], and Bourchard et al. [13]. They used different approaches using the finite element method to model the effect of concentration polarization on membrane permeability with laminar flow in a rectangular channel. Variable flux and incomplete salt rejection was considered, when predicting the concentration polarization effect in these studies.

However, less research has been conducted that consider the influence of surface morphology on predicting the concentration polarization effect. Diffusive transport is significant near the membrane, where concentration polarization boundary layers develop, whereas diffusive transport of smaller species in the bulk flow (outside the boundary layers) is generally negligible. In laminar cross-flow filtration, the transport of larger particles from the bulk into the boundary layer may be affected by interactions between particles and the fluid flow relatively far from the membrane surface. In particular, inertial lift arising from nonlinear interactions of particles with the surrounding flow field that may offset the drag force on particles associated with the flow of permeate across the membrane. The model described in this study is based on diffusion and hence takes into account particle interaction in the diffusive layer, where concentration polarization is anticipated to exist. It is proposed in this study that the surface morphology affects the retained solute concentration accumulating on the membrane film, thereby affecting permeate purity.

The objective of this study is to develop a new simulation method to evaluate the membrane surface morphology on mass transport and concentration polarization effect. It is assumed the mass permeating the membrane is not homogeneously diffused but varies with the localized thickness. Concentration polarization can be affected by the nonuniform film, leading to a nonhomogeneous diffusion within the concentration polarization layer. The simulation was performed using full-scale RO plant data collected from the water treatment plant operated by the city of Sarasota. For model development, the entire membrane channel is discretized into small slices with uniform size, then the localized surface thickness is incorporated into the model to determine the water qualities at each slice using a finite difference method. Finally, model validation is performed by comparing the actual salt permeate concentration to the prediction results.

2. Model development

Many different theories and models attempt to describe mass transfer in diffusion-controlled membrane processes [14–17]. However, a few basic principles or theories are used to develop most of these models: convection, diffusion, film theory, and electroneutrality. These principles or theories could be used to group models into homogeneous diffusion models, exponential diffusion models, and coupling models. In the homogeneous diffusion model, most of the parameters such as cross flow velocity, salt concentration, applied pressure, and osmotic pressure are assumed to be constant through the membrane channel [18]. The schematic of an RO channel is shown in Fig. 1. The simulation presented in this study depicts varied

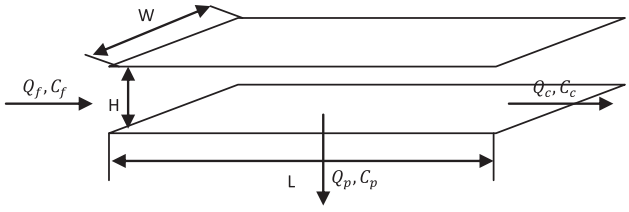

Fig. 1. Schematic representation of a membrane channel.

flow and concentration profiles along the membrane channel, demonstrating a more practical method for use in full-scale applications.

2.1. Mass transport

The RO membrane process can be represented by a filtration channel with permeate channel on one side and a sealed side on the other. The entire channel can be divided into small uniform slices, so the permeate flow rate (Q_{pi}) and salt permeate concentration (C_{pi}), bulk flow rate (Q_i) and bulk flow concentration (C_i) can be determined at each slice. The overall permeate concentration can be calculated with the mass transporting through the membrane divided by the permeate flow. The basic equations for model developing are shown in Eqs. (1)–(5). The principles are mass balance, flow balance, and mass diffusion. The product water flux (F_{wi}) is determined by the net driven pressure ($\Delta p_i - \Delta \pi_i$) and correlated with a mass transfer coefficient (k_{wi}). The permeate salt flux is calculated by the concentration gradient across the membrane film multiplied by a mass transfer coefficient (k_{si}). The uniform slice along the membrane channel is depicted in Fig. 2. In this representation, concentration polarization results in a higher salt concentration on the membrane surface than the bulk flow, and leads to Brownian back diffusion from the membrane surface.

The computational boundary is taken from one uniform slice of the membrane channel, in which i denotes the computational iteration along the membrane channel.

$$F_{wi} = k_{wi}(\Delta p_i - \Delta \pi_i) = \frac{Q_{pi}}{A_i} \tag{1}$$

$$J_i = k_{si}(C_i - C_{pi}) \tag{2}$$

$$Q_{pi} = Q_i - Q_{i+1} = -\Delta Q \tag{3}$$

$$Q_i C_i = Q_{pi} C_{pi} + Q_{i+1} C_{i+1} \tag{4}$$

Combining Eqs. (3) and (4), the relationship between C_i and C_{pi} can be derived as Eq. (5):

$$C_i + \Delta C = \frac{C_i + C_{pi}\frac{\Delta Q}{Q_i}}{1 + \frac{\Delta Q}{Q_i}} \tag{5}$$

where ΔC is the concentration difference across the uniform slice in the bulk flow and ΔQ is the volumetric flow difference across the uniform slice in the bulk flow.

Osmotic pressure is defined in Eq. (6):

$$\Delta \pi_i = k_t(C_i - C_{pi}) \tag{6}$$

where k_t equals $0.01\left(\frac{psi}{\frac{mg}{L}TDS}\right)$ [19]. The solute permeate concentration is equal to the permeate solute flux $\left(\frac{mg}{sfd}\right)$ over the permeate water flux $\left(\frac{L}{sfd}\right)$.

$$C_{pi} = \frac{J_i}{F_{wi}} \tag{7}$$

Approximating the net driven pressure ($\Delta p_i - \Delta \pi_i$) by assuming $k_t C_i \approx k_t(C_i - C_{pi})$, permeate flow rate can be estimated with Eq. (8):

$$Q_{pi} = \frac{k_{wi}(\Delta p_i - k_t C_i)}{A_j} \tag{8}$$

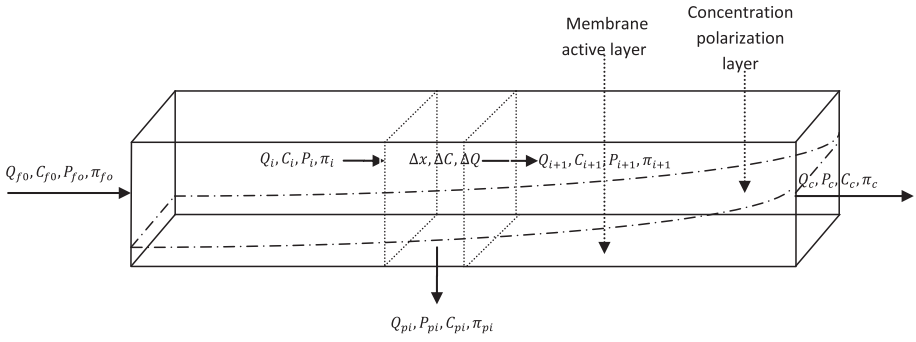

Fig. 2. Schematic representation of a computational slice of a membrane channel.

Combining Eqs. (1), (2), (6), and (7), the solute concentration at each uniform slice within the membrane module can be derived as Eq. (9):

$$C_i = \frac{C_{pi}k_{wi}\Delta p}{k_{si}} - \frac{C_{pi}k_{wi}k_t C_i}{k_{si}} + \frac{C_{pi}^2 k_{wi}k_t}{k_{si}} + C_{pi} \quad (9)$$

Approximating Eq. (9) using $\frac{k_{wi}\Delta p}{k_{si}} \gg \frac{k_{wi}k_t}{k_{si}}$, $C_i \gg C_{pi}$ [3], Eq. (9) can be simplified as:

$$C_{pi} = \frac{C_i}{1 + \frac{k_{wi}\Delta p}{k_{si}} - \frac{k_{wi}k_t C_i}{k_{si}}} \quad (10)$$

Assuming:

$$a_1 = 1 + \frac{k_{wi}\Delta p_i}{k_{si}} \quad (11-\text{a})$$

$$a_2 = \frac{k_{wi}k_t}{k_{si}} \quad (11-\text{b})$$

The permeate concentration can be determined by Eq. (12):

$$C_{pi} = \frac{C_i}{a_1 - a_2 C_i} \quad (12)$$

Therefore, the solute permeate concentration can be found in terms of concentration at the bulk flow (C_i), water and solute MTCs (k_{wi}, k_{si}), and the transmembrane pressure at each uniform slice. Substituting Eq. (12) into Eq. (5) and rearranging:

$$\frac{\Delta C}{C_i} + \frac{\Delta Q}{Q_i} + \frac{\Delta C \Delta Q}{C_i Q_i} = \frac{\Delta Q}{Q_i(a_1 - a_2 C_i)} \quad (13)$$

Approximating Eq. (13) using $\frac{\Delta C \Delta Q}{C_i Q_i} \approx 0$, Eq. (14) can be derived.

$$\frac{\Delta C}{C_i\left(\frac{1}{a_1 - a_2 C_i} - 1\right)} = \frac{\Delta Q}{Q_i} \quad (14)$$

When the numerical solution of Eq. (14) is obtained by the finite difference method, the discrete form of Eq. (14) is as follows:

$$C_{i+1} = \frac{Q_{pi}}{Q_i} C_i \left(1 - \frac{1}{a_1 - a_2 C_i}\right) + C_i \quad (15)$$

Q_{pi} can be solved by Eq. (8) and Q_i can be calculated from cross flow velocity (v_i) in the membrane channel. The cross flow velocity can be expressed in the following:

$$v_i = \frac{Q_i}{WH} \quad (16)$$

where W is the membrane element width and H is the channel height. As feed flow travels in the membrane channel, transmembrane pressure decreases due the hydraulic head loss. The transmembrane pressure profile in the membrane channel can be described by Eq. (17) [13]:

$$\Delta P_i = (P_f - P_p) - \frac{12k\mu v_i L}{nH^2} \quad (17)$$

Where P_f and P_p is the feed and permeate pressure, k is the friction coefficient, μ is the fluid viscosity, L is the membrane channel length, and n is the number of uniform slices for channel discretization. With a known pressure at the end of the membrane channel and assuming the permeate pressure stays constant, the friction coefficient can be determined in Eq. (18):

$$k = \frac{(P_f - P_c)H^2}{12\mu v_c L} \quad (18)$$

where P_c is the concentrate pressure and v_c is the cross flow velocity at the end of membrane channel. Eq. (17) is substituted into Eq. (11 – a) for the subsequent calculation. The salt concentration in the bulk flow and permeate concentration can be solved using Eqs. (15) and (12) with the initial conditions:

$$C_0 = C_f;\ Q_0 = Q_f;\ \Delta P_0 = P_f - P_p \quad (19)$$

2.2. Concentration polarization

When water permeates a pressure driven membrane, the retained solutes tend to accumulate at the membrane surface and create a concentration gradient between the bulk and the membrane surface. This concentration gradient will result in a diffusion of salts from the membrane surface to the bulk. This phenomenon is referred to as concentration polarization. In the RO membrane process, concentration polarization leads to an increase in the osmotic pressure and thereby reduces the permeate flux. The expression of concentration polarization at steady state is given by [20]:

$$\frac{C_{mi} - C_{pi}}{C_i - C_{pi}} = \exp^{\frac{F_w \delta}{D}} = \exp^{\frac{F_w}{k_d}} \quad (20)$$

where C_{mi} is the concentration at the membrane surface, δ is the thickness of concentration polarization layer, D is the diffusivity of salt, and k_d is the mass transfer coefficient. The concentration difference across the membrane film can be calculated with Eq. (21):

$$dc = C_{mi} - C_{pi} = (C_i - C_{pi}) \exp^{\frac{F_w}{k_d}} \quad (21)$$

k_d can be related to the cross flow velocity and the geometry of the membrane channel by means of the following dimensionless analysis under laminar flow condition [21]:

$$\mathrm{Sh} = 1.86\mathrm{Re}^{0.33} Sc^{0.33} = \frac{k_d d_h}{D} \quad (22)$$

$$\mathrm{Re} = \frac{v_i d_h \rho}{\mu} \quad (23)$$

$$S_c = \frac{\mu}{D_\rho} \quad (24)$$

where d_h is the hydraulic diameter of the membrane channel; ρ is the water density; D is the salt diffusivity. Combining Eqs. (22)–(24), the mass transfer coefficient k_d can be calculated with Eq. (25):

$$k_d = 1.86\left(\frac{D}{dh}\right)^{0.67} (v_i)^{0.33} \quad (25)$$

Substituting Eq. (21) into Eq. (12), inserting the result of $\boldsymbol{k_d}$, and assuming $C_{pi} \ll C_i < C_{mi}$, the salt permeate concentration can be determined by Eq. (26):

$$C_{pi} = \frac{C_i \exp^{\frac{F_w}{k_d}}}{a_1 - a_2 C_i \exp^{\frac{F_w}{k_d}}} \quad (26)$$

2.3. Mass transfer coefficients — k_{si}, k_{wi}

AFM images show the membrane surfaces are nonuniform with varied thickness along the surface [22–23], and therefore, mass transport through the membrane surface can be considered as nonhomogeneous. It is assumed a faster transport occurs at the valleys, where the activation energies are less than the ridges. Therefore, mass transfer at the valleys will contribute the majority of mass passage in the permeate stream. The original idea of nonhomogeneous diffusion as applied to synthetic membranes is, in part, derived from research performed by Duranceau, who studied the permeate transient response in nanofiltration membrane processes [24]. The transient permeate response to a concentration gradient change was modeled using a homogeneous diffusion model but it was noted that deviations in model prediction occurred, when the transients had been reversed. It was suspected that additional interactions may have affected the means of solute mass transfer through the membrane film, but for the cause of the variations could not be identified at that time. Advancements in the understanding of the surface morphology of the active membrane layer allowed the nonhomogeneous diffusion to be further explored in this study.

Previous diffusion models typically assumed a constant mass transfer across a nonporous, smooth, flat membrane surface, where solute and solvent permeability is driven by the concentration and pressure gradient that exists between the feed and permeate sides of the membrane. However, nonhomogeneous mass transfer introduces an additional variable affecting mass transport that can quantified by considering the nonuniform structure of the membrane surface.

Research conducted by Song and colleagues demonstrated that random distribution models can be used to describe heterogeneity of surfaces [22]. This mathematical approach was used to quantitatively describe the random distribution of the membrane's surface roughness. Continuous random heterogeneity would indicate that sites of ridge-and-valley morphology are randomly distributed over the entire surface of the membrane. The Gaussian distribution presented in Eq. 27 can be used to numerically represent the active layer by a white random vector (w).

$$P(w) = \frac{1}{\sigma\sqrt{2\pi}} \exp\left[-\frac{(w-\mu)^2}{2\sigma^2}\right] \quad (27)$$

where μ is the mean and σ is the standard deviation of the random vector (w). Similarly, the variations in membrane thickness can be approximated by a Gaussian distribution. Because the mass transfer coefficients (MTCs) k_{si} and k_{wi} are affected by the membrane thickness, they can be approximated with the same distribution as the membrane thickness. This is expressed in Eq. (28). Substituting Eq. (28) into Eq. (26), the permeate concentration will be determined by the concentration at the membrane surface and the membrane thickness.

$$P(k_{si}, k_{wi}) = \frac{1}{\sigma_{s,w}\sqrt{2\pi}} \exp\left[-\frac{(k_{si,wi} - \overline{k_{s,w}})^2}{2\sigma_{s,w}^2}\right] \quad (28)$$

In Eq. (28), $\overline{k_s}$, $\overline{k_w}$ are the mean values of solute and solvent MTCs and can be determined by fitting the plant data into Eqs. (1) and (2). $\sigma_{s,w}$ can be estimated by the thickness variation that related to the actual membrane images produced by AFM. The AFM images of two types of RO membranes manufactured by Hydranautics (Oceanside, CA), namely the ESPA2 and the CPA3 membranes, are shown in Figs. 3 (a) and 3(b), respectively.

In Fig. 3, the average of the RO membrane thickness, provided by the manufacturer, is about 200 nm. The variation of ESPA2 and CPA3 is about 400 and 300 nm, respectively. According to the manufacturer the AFM images are representations of the membrane film, and that the membrane surface topography can be assumed to be consistent across each element. The standard deviation (estimated at 200 and 150 nm) will produce morphology visually comparable to the AFM images using the "NORMRND" function embedded in MATLAB with a "SMOOTH" script to reduce the influence of outlying data. The size of the random vector used to generate the membrane surface is the same as the number of uniform slices (n) for channel discretization. The hypothetical membrane surfaces generated by MATLAB are depicted in Figs. 4(a) and 4(b).

Figs. 4(a) and 4(b) depict membranes with surface roughness similar to the AFM membrane images provided by Hydranautics (Oceanside, CA) in Figs. 3(a) and 3(b). Figs. 4(a) and 4(b) appear to be visually comparable to Figs. 3(a) and 3(b), respectively. Based on this similarity, the MTCs k_{si}, k_{wi} can be correlated to surface random vector (w) with a coefficient $\theta_{s,w} = \frac{\overline{k_s}.\overline{k_w}}{\mu_w}$. Therefore, $\sigma_{s,w}$ can be calculated with Eq. (29) and k_{si}, k_{wi} can be solved by Eq. (28).

$$\sigma_{s,w} = \theta_{s,w}\sigma_m \quad (29)$$

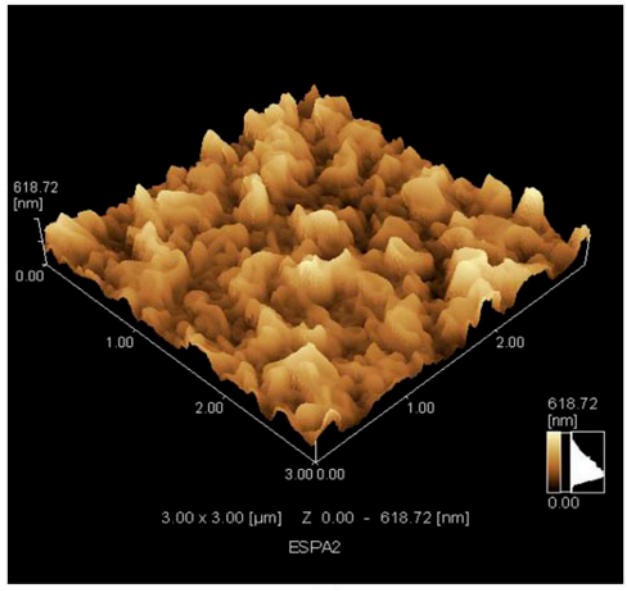

(a)

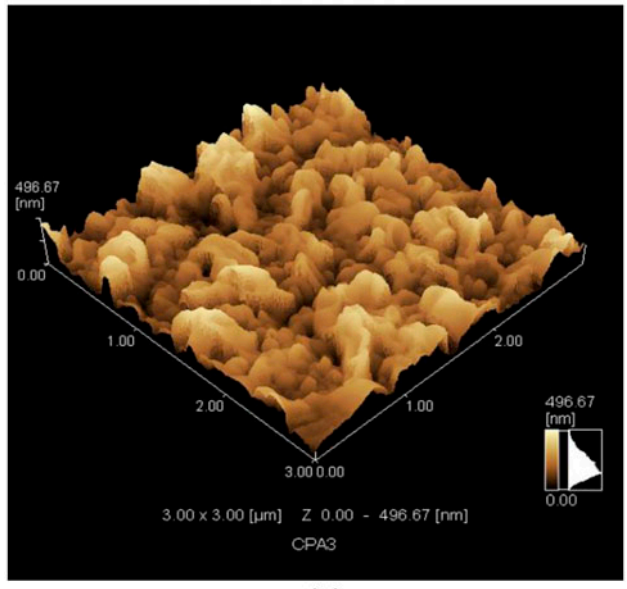

(b)

Fig. 3. AFM imagines of ESPA2 (a) and CPA3 (b) RO membranes (Courtesy of Hydranautics, Oceanside, CA).

3. Results and discussion

3.1. Full-scale plant data

The simulation was conducted using data collected from the city of Sarasota's 4.5 MGD brackish groundwater membrane desalination process that is located along Florida's southwest coast. The city's RO plant consists of three process skids, where each skid is arranged in a 2–1 array containing twenty-eight eight-inch diameter six-element pressure vessels (PVs) in the first stage and fourteen eight-inch diameter six-element PVs in the second stage. The city of Sarasota provided information obtained from more than eight years of continuous RO process operation, that included feed, permeate, and concentrate stream pressure, conductivity, flow rate, and recovery data. The permeate flow and salt passage data were normalized according to ASTM standards using, in part, data presented in Table 1 [18]. Additional details regarding the city of Sarasota's process can be found in study conducted by Tharamapalan and co-workers [25].

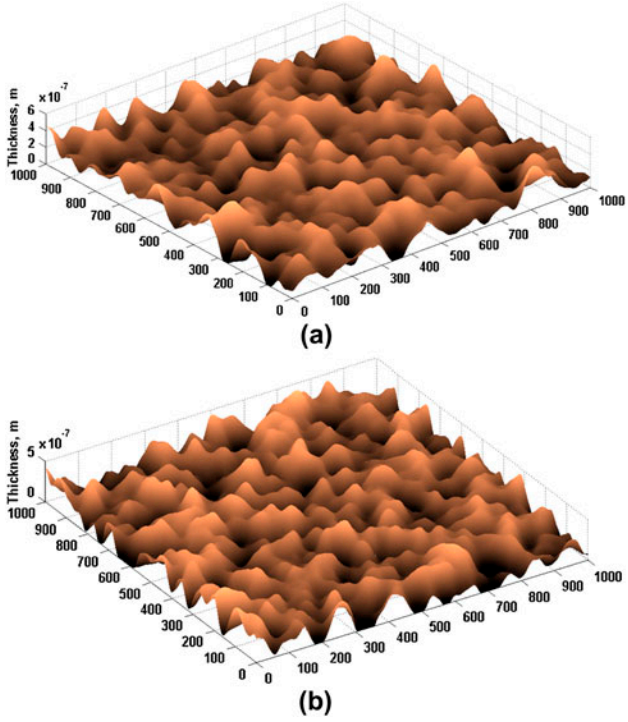

Fig. 4. Numercial plot of membranes surface stuctures of (a) ESPA2; (b) CPA3. Note that *X*- and *Y*-coordinates are the size of the random vector (*Z*), with the *Z*-coodinate representing membrane thickness.

As shown in Table 1, the full-scale RO system utilizes two different types of membranes manufactured by Hydranautics (Oceanside CA). The corresponding membrane surfaces, shown in Figs. 4(a) and 4(b), and were used for subsequent model fitting and validation. From over 5,040 data points available, 70% were used for model fitting and the remaining 30% were used for simulation. The parameters used in the simulation are listed in Table 2. The normalized water mass transfer coefficient ($\bar{k}_w$) was obtained by fitting the permeate flux over the pressure difference across the membrane, as described by Eq. (1), and the normalized salt mass transfer coefficient ($\bar{k}_s$) was obtained by fitting the salt permeate flux over the concentration difference across the membrane, as described by Eq. (2). The diffusivities of salts were calculated by averaging the ions diffusivities with weighting factors in the feed stream.

3.2. Numerical simulation

A numerical simulation was implemented initially to develop the concentration and flow profiles in the membrane channel. This incremental representation of the flow rate through each uniform slice of the membrane element allows for simulation of the solute concentration profile. Using the parameters listed in Table 2, the MTCs k_{si} and k_{wi} can be determined by localized thickness, as shown in Figs. 5 and 6. Figs. 5 and 6 depict the effect of thickness variation on the solute and solvent MTCs for both types of membrane used within the full-scale process. The peak and bottom of k_{si} and k_{wi} can be related to the valleys and ridges on membrane surface. It is reasoned the rate mass transport at the valleys of a membrane surface is faster that contributes the majority of mass permeating the membrane, while the transport of mass retained at the ridges will pass through the membrane at a lower rate.

When k_{si} and k_{wi} are solved, the permeate flow (Q_{pi}) can be simulated along the membrane channel with the average of feed flow and concentration as the initial condition for simulation, shown in Fig. 7. With increasing axial distance, the overall trend of permeate flow decreases along the membrane channel as a result of the combination effect of pressure head loss and enhanced osmotic pressure. However, this effect is reduced by the thickness variation, where a higher permeate flow occurs at the valleys.

Figs. 8(a) and 8(b) describe the effect of the concentration polarization layer on the concentration profile between the bulk flow (C_i) and membrane surface (C_{mi}) for each stage. As the solute is incompletely retained by the membrane, the solute concentration in the bulk flow and on the membrane surface increases along the membrane channel but at a slower pace than the first stage. It is also observed that the concentration difference between C_i and C_{mi} increases in the second stage due to higher feed concentration and higher surface variation. This can lead to significant cake deposit on the membrane and reduce the permeate flux. Once k_{si}, C_{mi}, and Q_{pi} are solved, the permeate concentration (C_{pi}) along the membrane channel can be determined using Eq. (26). The permeate concentration is plotted in Figs. 9(a) and 9(b). Both clearly show the permeate concentration increases along the membrane channel. This suggests that a higher salt passage occurs at the end of the membrane channel as a result of an increased concentration polarization effect in the cross flow direction. Moreover, Fig. 9(b) shows a larger concentration variation between the ridge and valley than Fig. 9(a), indicating the membrane used for the first stage (CPA3) has a smoother surface than the one used for the second stage (ESPA2-LD). This observation is consistent with information provided by the manufacturer (Fig. 3).

Table 1
City of Sarasota RO process overview

Parameter	Unit	1st stage	2nd stage
Manufacturer	–	Hydranautics	Hydranautics
Membrane type		CPA3/RO	ESPA2-LD/RO
Element area	sq ft	400	400
Permeate flow	gpd	1,000,000	400,000
Recovery	%	54	44
Feed pressure	psi	180	145
Feed TDS	mg/L	1967	4,028
Conductivity	μs/cm	3,242	8,184
Feed pH	–	5.8	5.8
Temperature	℃	26–29	26–29

Table 2
Parameters for simulation

Parameter	Unit	1st stage	2nd stage
Water density (25℃)	kg/m^3	997×10^3	997×10^3
Water viscosity (25℃)	$N\,s/m^2$	0.89×10^{-3}	0.89×10^{-3}
Diffusivity of salts	m^2/s	1.29×10^{-9}	1.27×10^{-9}
Feed channel height	m	7.9 × 10–4	8.6×10^{-4}
Total length of channel	m	4.69	4.86
Channel width	m	0.917	0.917
Number of leaves	–	26	25
Average velocity	m/s	0.12	0.11
Reynolds number (Re)	–	208	214
Water ($\overline{K}_w$)	m/s-ψ	5.37×10^{-8}	7.52×10^{-9}
TDS ($\bar{k}_s$)	m/s	6.18×10^{-8}	5.53×10^{-8}
Number of uniform slice	–	1,000	1,000

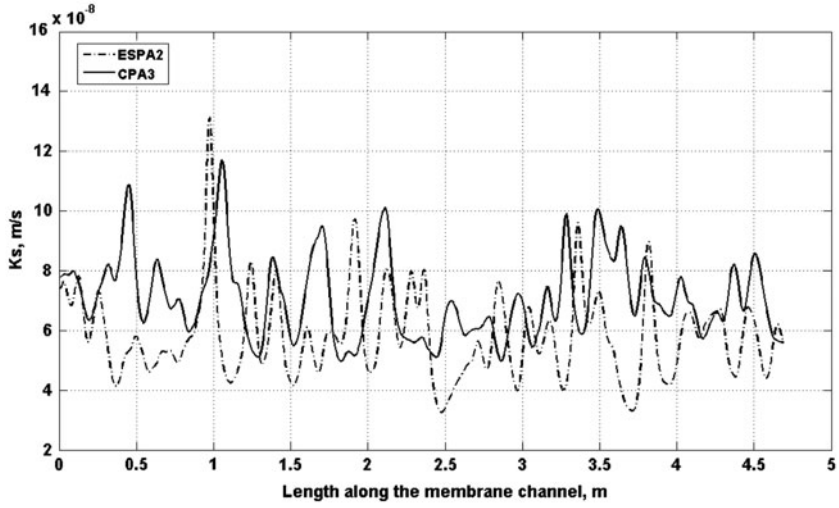

Fig. 5. Simulation of solute mass transfer coefficient for CPA3 RO membrane (first stage) and ESPA2-LD RO membrane (second stage).

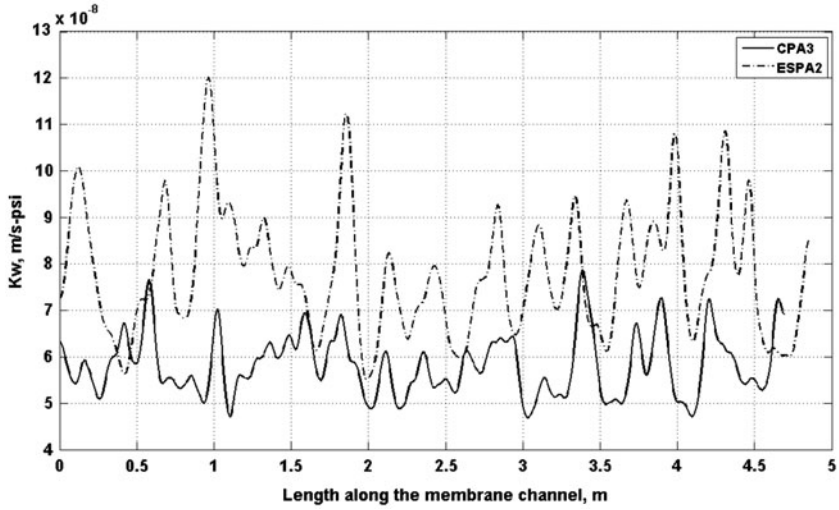

Fig. 6. Simulation of solvent mass transfer coefficient for CPA3 RO membrane for the first stage and ESPA2-LD RO membrane for the second stage.

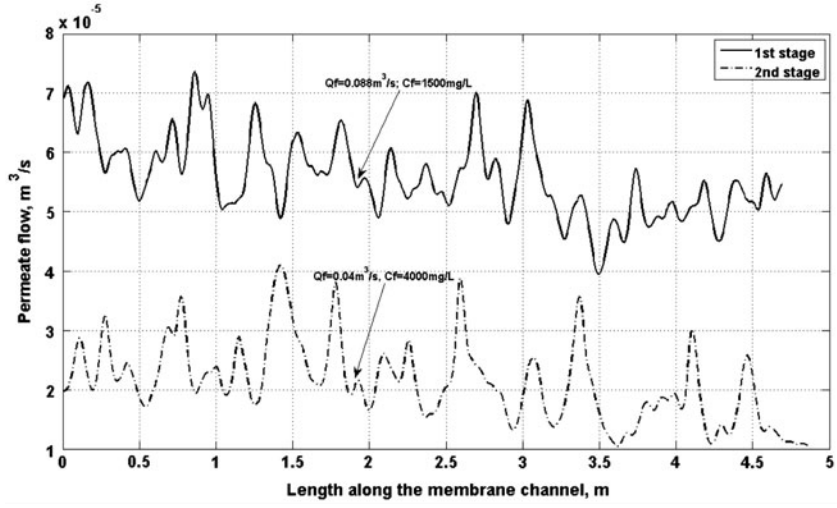

Fig. 7. Simulation of permeate flow along the membrane channel.

3.3. Model validation

The prediction of permeate concentration is determined by the total mass permeating the membrane divided by the permeate flow rate. Results of the model validation are presented in Fig. 10 showing predicted versus actual plots for each stage. The solid line in Fig. 10 represents the ideal line, where no error is observed between predicted and actual data. The simulation results clustered around the solid line indicating a good prediction. Further model validation was performed through calculation of the average percentage of difference (APE) between actual and predicted permeate TDS concentrations. APE is defined as the percentage of absolute difference between the actual and predicted concentration divided by the actual concentration. Initially, the APE was averaged on a weekly basis for each model, by stage, shown in Figs. 11(a) and 11(b). Fig. 11 illustrates that the weekly APEs appear to aggregate in a lower and narrower range for the first stage, when compared with the second stage but most predictions by both stages are within 5 to 15% of the APE. The deviations between actual and predicted values may have been partially caused by plant process operations, when rotation of the source water causes variation of salt composition in feed water or alteration of applied pressure to maintain a constant recovery.

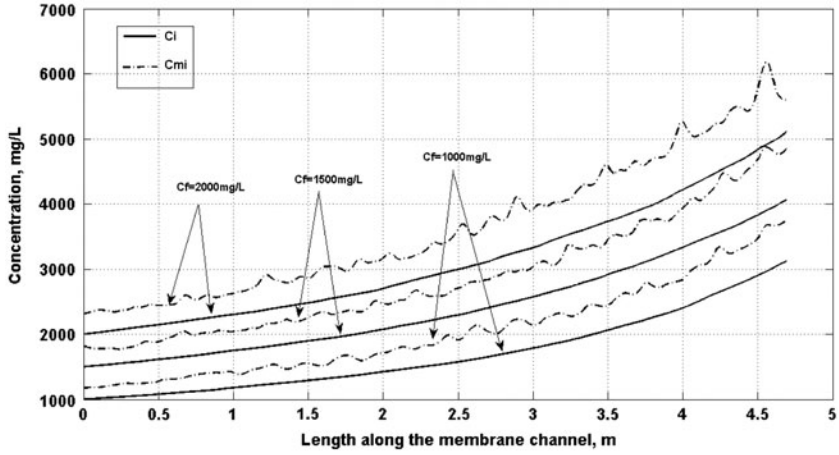

Fig. 8(a). Simulation of solute concentration in the bulk flow and on membrane surface along the membrane channel in the first stage.

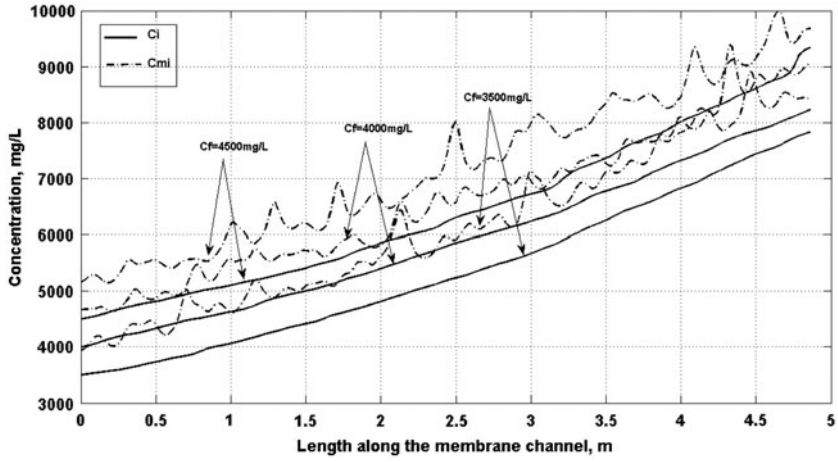

Fig. 8(b). Simulation of solute concentration in the bulk flow and on membrane surface along the membrane channel in the second stage.

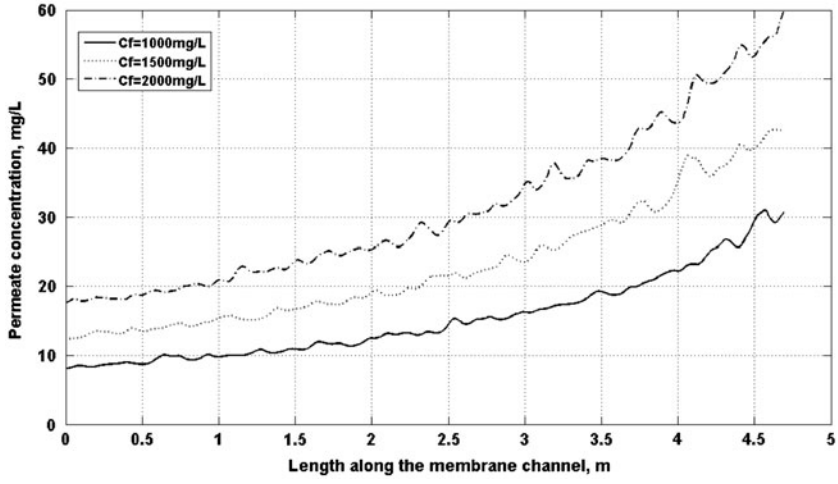

Fig. 9(a). Simulation of TDS permeate concentration along the membrane channel for the first stage.

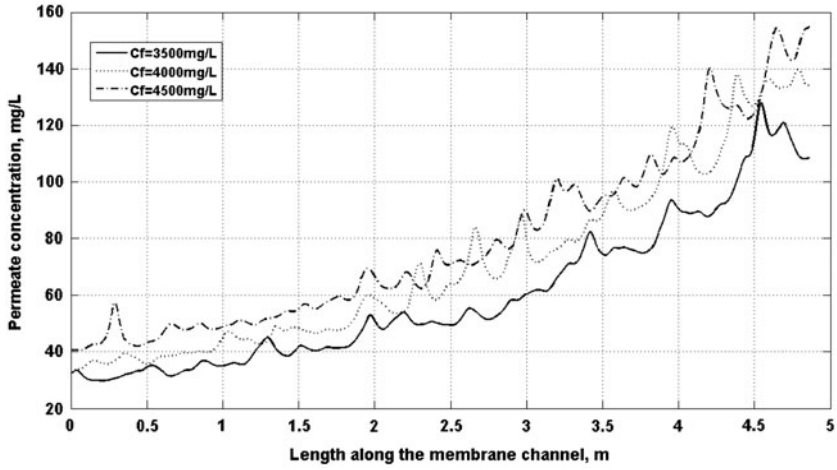

Fig. 9(b). Simulation of TDS permeate concentration along the membrane channel for the second stage.

4. Conclusions and recommendations

Several mathematical models have been postulated or developed over the years for describing solute and solvent mass transport in membrane processes based on a homogeneous membrane surface. In this study, the effects of the uneven, ridge, and valley morphology of the membrane active layer on solute mass transport was investigated. It was determined that solute mass transport is controlled by nonhomogeneous diffusion in the thinner regions (membrane valleys) of the active layer. This nonuniform surface also affects the concentration polarization layer, where more solutes tend to accumulate on the valleys than on the ridges. Mathematically, the uneven RO membrane active layer was approximated by Gaussian distribution with a specified mean value and standard deviation. Simulations were performed based on this surface property and solved using a finite difference method to numerically investigate the nonhomogeneous phenomenon. As a result, the MTCs (k_{si}, k_{wi}) were simulated in the cross flow direction to predict the permeate flow profile, retained solute concentration gradient in the bulk flow and on the membrane surface, and the permeate concentration gradient within the membrane permeate channel.

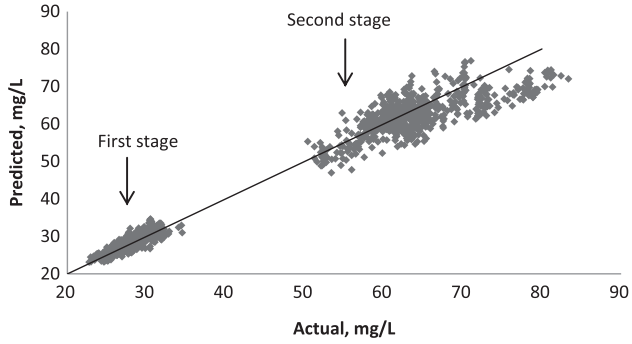

Fig. 10. Comparison of actual and simulated TDS concentration in permeate flow for both stages.

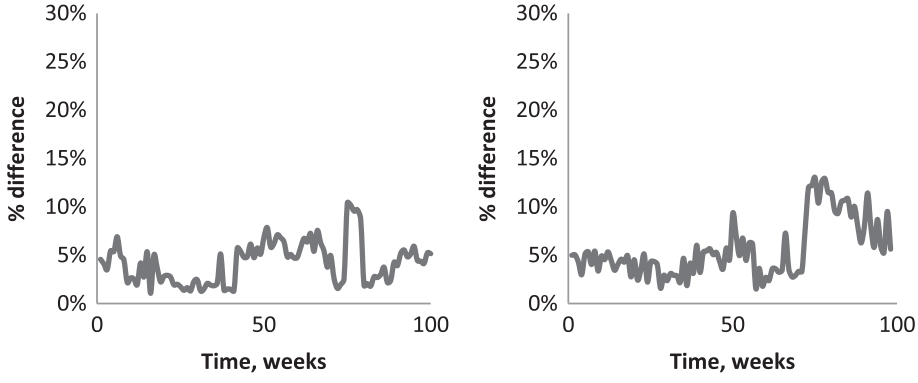

Fig. 11. APE between actual and simulated TDS concentration in permeate flow. (a) first stage; (b) second stage.

A simulation was performed with full-scale data from a 4.5 million gallon per day brackish groundwater RO membrane process located in the city of Sarasota, Florida. Feed TDS concentration, feed flow, and feed applied pressure were used as initial conditions for solving the mass transport equation in Eqs. (16) and (26). Predicted TDS permeate concentration was compared with the monitored plant data through development of predicted versus actual plots and calculation of APE. The results demonstrated that the surface morphology has impacted the permeate flow profile, the concentration gradient on the membrane surface, and the concentration gradient within the permeate channel. A smoother surface indicated a less deviation in permeate flow profile and concentration gradient across the membrane film, thereby reducing the fouling potential.

However, because the model that was developed in this research was based on the conditions of the City of Sarasota's membrane process, this study should be repeated at another facility to determine overall applicability across a broader range of conditions. For example, the model could be evaluated for those conditions experienced in nanofiltration or seawater membrane operations, as well as other similar brackish groundwater applications.

Further development of this model could be conducted by incorporating membrane properties, such as surface charge or membrane hydrophilicity into the modeling approach. Also, the role that different foulants play on the surface topography could be further studied using the approach established in this current study in order to determine impacts of surface morphology with respect to changes in solute and solvent MTCs over time.

Acknowledgments

The research was funded, in part, by UCF's Research Foundation through a grant provided by the Jones Edmunds Research Fund (Project 05-1620-0002 – RF1047820), as well as Funding Agreement 16208081 with the city of Sarasota, Florida. Any opinions, findings, and conclusions expressed in this material are those of the authors and do not necessarily reflect the views of UCF (Orlando, FL), its Research Foundation, Jones Edmunds Associates, Inc. (Gainesville, FL) or the city of Sarasota, Florida. The mention of trade names or commercial products does not constitute endorsement or recommendation. The authors acknowledge the contribution of Hydranautics (Oceanside, CA) in their providing UCF with AFM membrane images, without which this study would not have been made possible. The authors would like to thank Mr. Javier Vargas, Mr. Peter Perez, Ms. Katherine Gussie, and Mr. Gerald Boyce of the City of Sarasota's Public Works and Utilities Division (Sarasota, FL) for providing full-scale reverse osmosis membrane process operations data that was relied upon for model development and validation.

Symbols and abbreviations

i	—	the number of computational iteration along the channel
A_i	—	uniform slice area in permeate flow direction, m^2
C_f	—	feed concentration, mg/L
C_{pi}	—	permeate concentration, mg/L
C_i	—	concentration in the bulk flow, mg/L
C_{mi}	—	concentration on the membrane surface, mg/L
dc	—	concentration difference across the membrane film, mg/L
ΔC	—	concentration difference Across the uniform slice in the cross flow direction, mg/L
D	—	diffusivity of salts, m^2/s
dh	—	hydraulic diameter, m
F_{wi}	—	solvent permeate flux, gal/sfd
H	—	membrane channel height, m
J_i	—	solute permeate flux, mg/sfd
k_d	—	back diffusion coefficient, m/s
$\overline{k}_s$	—	overall mass transfer coefficient for salt, m/s
$\overline{k}_w$	—	overall mass transfer coefficient for water, m/s-ψ
k_{wi}	—	solvent mass transfer coefficient, m/s-ψ
k_{si}	—	solute mass transfer coefficient, m/s
k_t	—	0.01 ψ/(mg/L TDS)
L	—	membrane channel length, m
n	—	amount of uniform slice for channel discretization
Δp	—	transmembrane pressure, ψ
$\Delta\pi$	—	osmotic pressure, ψ
Q_f	—	feed flow, m^3/s
Q_c	—	concentration flow, m^3/s
Q_{pi}	—	permeate flow, m^3/s
Q_i	—	flow in the membrane channel, m^3/s
ΔQ	—	flow difference across the uniform slice in the cross flow direction, m^3/s
Re	—	Reynolds number
Sh	—	Sherwood number
Sc	—	Schmidt number
r_i	—	recovery at uniform slice, %
$\mu_{s,w}$	—	mean of random vector
v_i	—	cross flow velocity, m/s
$\sigma_{s,w}$	—	standard deviation of random vector

ρ — density of water, kg/m^3
W — membrane channel width, m
w — random vector with Gaussian distribution
μ — dynamic viscosity of water, $N\ s/m^2$
δ — thickness of concentration polarization layer, m

References

[1] Y. Zhao, J.S. Taylor, Incorporation of osmotic pressure in an integrated incremental model for predicting RO or NF permeate concentration, Desalination 174 (2005) 145–159.
[2] Y. Zhao, J.S. Taylor, Assessment of ASTM D 4516 for evaluation of reverse osmosis membrane performance, Desalination 180 (2005) 231–244.
[3] K. Jamal, M.A. Khan, M. Kamil, Mathematical modeling of reverse osmosis system, Desalination 160 (2004) 29–42.
[4] Y. Zhao, J.S. Taylor, S. Chellam, Predicting RO/NF water quality by modified solution diffusion model and artificial neural networks, J. Membr. Sci. 263 (2005) 38–46.
[5] S.A. Avlonitis, D.G. Pavlou, S. Skourtis, Simulation of the spiral wound RO membranes deformation under operating conditions, Desalin. Water Treat. 25 (2011) 91–97.
[6] N.Y. Yip, A. Tiraferri, W.A. Phillip, J.D. Schiffman, M. Elimelech, High performance thin-film composite forward osmosis membrane, Environ. Sci. Technol. 44 (2010) 3812–3818.
[7] S. Bason, Y. Oren, V. Freger, Characterization of ion transport in film using electrochemical impendance spectroscopy II: Examination of the polyamide layer of RO membranes, J. Membr. Sci. 302 (2007) 10–19.
[8] J. Mendret, C. Guigui, C. Cabassud, P. Schmitz, Numerical investigations of the effect of non-uniform membrane permeability on deposit formation and filtration process, Desalination 263 (2010) 122–132.
[9] Y. Zhao, J. Taylor, S. Hong, Combined influence of membrane surface properties and feed water qualities on RO/NF mass transfer, a pilot study, Water Res. 39 (2005) 1233–1244.
[10] E.M. Vrijenhoek, S. Hong, M. Elimelech, Influence of membrane surface properties on initial rate of colloidal fouling of reverse osmosis and nanofiltration membranes, J. Membr. Sci. 188 (2001) 115–128.
[11] P.L. Brain, Concentration polarization in reverse osmosis desalination with variable flux and incomplete salt rejection, I&EC Fundam. 4(4) (1965) 439–445.
[12] B.J. Marinas, A. Member, R.I. Urama, Modeling concentration-polarization in reverse osmosis spiral-wound elements, J. Environ. Eng. 122(4) (1996) 292–298.
[13] C.R. Bouchard, P.J. Carreau, T. Matsuura, S. Sourirajan, Modeling of ultrafiltration: Prediction of concentration polarization effect, J. Membr. Sci. 97 (1994) 215–229.
[14] Y. Zhao, Modeling of Membrane Solute Mass Transfer in NF/RO System Membrane Systems, PhD Dissertation, University of Central Florida, Orlando, FL, 2004.
[15] S.S. Chen, Modeling of Membrane Surface Chemistry and Mass Transfor, PhD Dissertation, University of Central Florida, Orlando, FL, 1999.
[16] L-K. Sung, Film-theory and Ion Coupling models For Diffusion Controlled Membrane Processes, PhD Dissertation, University of Central Florida, Orlando, FL, 1993.
[17] J.S. Taylor, E.P. Jacobs, Reverse osmosis and nanofiltration, in: J. Malleviablle, P.E. Odendaal, M.R. Wiesner (Eds.), Water Treatment Membrane Process, McGraw-Hill, New York, NY, 1996, pp. 9.1–9.70.
[18] L. Song, S. Hong, J.Y. Hu, S.L. Ong, W.J. Ng, Simulation of full-scale reverse osmosis membrane process, J. Environ. Eng. 128(10) (2002) 960–966.
[19] Standard practice for standardizing reverse osmosis performance data, Annual Book of ASTM Standards, D4516–65, West Conshohocken, PA, 2010.
[20] M.R. Wiesner, R. Aptel, Mass transport and permeate flux and fouling in pressure-driven process, in: J. Mallevialle, P.E. Odendaal, M.R. Wiesner, Water Treatment Membrane Processes, McGraw-Hill, New York, NY, 1996, pp. 4.1–4.30.
[21] M. Isaacson, A. Sonin, Sherwood number and friction factor correlations for electrodialysis system, with application to process optimization, Ind. Eng. Chem., Process Des. Dev. 15 (2) (1976) 313–321.
[22] L. Song, P. Johnson, M. Elimelech, Kinetics of colloid deposition onto heterogeneously charged surfaces in porous media, Environ. Sci. Technol. 28 (1994) 1164–1171.
[23] A. Mohammad, N. Hilal, L. Pei, Atomic force microscopy as a tool for asymmetric polymeric membrane characterization, Sains Malaysiana 40(3) (2011) 237–244.
[24] S.J. Duranceau, Modeling the permeate transient response to pertubation from steady state in a nanofiltration process, Desalin. Water Treat. 1(1) (2009) 7–16.
[25] J. Tharamapalan, C. Boyd, S. Duranceau, 3-step approach towards evaluation and elimination of acid use in pertreatment for a brackish water reverse osmosis process, J. Environ. Manage. 124 (2013) 115–120.